Particle Swarm Optimization-Based Parameter Design Method for S/*CLC*-Compensated IPT Systems Featuring High Tolerance to Misalignment and Load Variation

Yousu Yao, *Student Member, IEEE*, Yijie Wang, *Senior Member, IEEE*, Xiaosheng Liu, *Member, IEEE*, Yu Pei, Dianguo Xu, *Fellow, IEEE*, and Xiufang Liu

***Abstract*—Inductive power transfer (IPT) systems designed with conventional methods offer optimum performance only at specific operational points. These methods are not applicable for dynamic IPT systems where both the coupling and load change throughout the operation. This study proposes a novel particle swarm optimization (PSO)-based parameter design method and aims to obtain a steady output voltage regardless of the coupling and load. The proposed method addresses the constraints of the conventional methods where the compensation capacitors/inductors are designed to resonate with certain other inductors/capacitors at the system's operational frequency. The S/*CLC* (primary series, secondary capacitor–inductor–capacitor) compensation topology is chosen in this research as it offers many appealing characteristics. The procedure to design an IPT system using the proposed method is presented. Two IPT systems, one designed with the proposed scheme and the other using conventional methods, are theoretically and experimentally compared in terms of fitness, voltage variation ripple (VVR), and power transfer efficiency (PTE). It is demonstrated that the fitness and the VVR of the conventional system are 1400.8% and 372.3% higher than those of the proposed system.**

***Index Terms*—Inductive power transfer (IPT), load-independent output voltage, misalignment tolerance, particle swarm optimization (PSO), S/*CLC* compensation topology.**

I. Introduction

TRANSFERRING power using conductors has many challenges in niche applications, such as dynamic electric vehicle charging, biomedical implants, and underwater electrical

Manuscript received June 5, 2018; revised August 6, 2018; accepted September 9, 2018. Date of publication September 13, 2018; date of current version April 20, 2019. This work was supported by the Self-Planned Task of the State Key Laboratory of Robotics and System (HIT) under Grant SKLRS201808B. Recommended for publication by Associate Editor O. Lucia. *(Corresponding author: Yijie Wang.)*

Y. Yao, Y. Wang, Y. Pei, and D. Xu are with the State Key Laboratory of Robotics and System, Harbin Institute of Technology, Harbin 150001, China (e-mail:

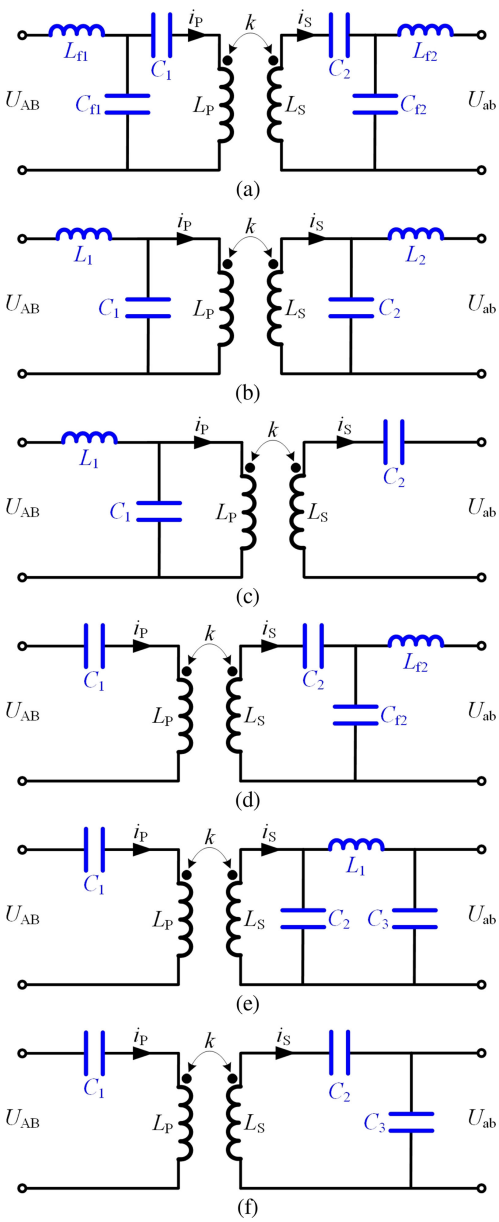

Fig. 1. Compensation topologies offering the characteristic of load-independent output voltage or current. (a) Double-sided *LCC*. (b) Double-sided *LCL*. (c) *LC*/S. (d) S/*LCC*. (e) S/*CLC*. (f) S/SP.

LCL [5], *LC*/S [6], S/*LCC* [7], S/*CLC* [8], and S/SP [9]. For the sake of clarity, these compensation topologies are displayed in Fig. 1, where the compensation components are highlighted with blue symbols and labels. The letters "*L*," "*C*," "S," and "P" denote "inductor," "capacitor," "series," and "parallel," respectively. The symbol "/" is the demarcation between the primary side and the secondary side. The characteristic of load-independent output voltage or current only holds when the operational coupling coefficient is equal to the designed coupling coefficient. Apparently, this condition cannot be guaranteed in all cases.

Several investigations attempted to improve the stability of the output power against coupling variations by improving the conventional parameter selection methods [10]–[12]. As a result, various novel parameter design methods were proposed. The IPT systems designed with these new methods offer much higher tolerance to misalignments. However, these schemes do not adequately address output power variations against coupling variations in the case of varying loads. For a practical system, the output power should be steady within a given tolerance for the entire range of coupling and load variation.

Apart from proposed compensation topologies and parameter design methods, some investigations took strides to solve this issue by constructing high-misalignment magnetic structures. Numerous novel structures, including double-D (DD) and double-D and quadrature (DDQ) coupler [13], bipolar (BP) pad [14], unsymmetrical circular coil pad [15], multithread rectangle-shaped coil [16], tetrahedron-type pickup mechanism [17], three-dimensional (3-D) orthogonal ferrite coils [18], and asymmetric coil sets [19], are put forward. In order to obtain a steady output voltage or current, a suitable magnetic coupling structure is necessary. Even though the authors firmly believe in this requirement, magnetic design is excluded from this paper due to space limitations.

Pre-regulation dc–dc converters on transmitter side and post-regulation dc–dc converters on receiver side are the two most frequently utilized methods to reduce the output voltage ripple against the coupling coefficient and load resistance. Nevertheless, wireless communication between the primary and secondary sides is required if a pre-regulation converter is employed. Accordingly, the cost of the IPT system increases, and the dynamic performance of the IPT system deteriorates. These two drawbacks can be overcome if a post-regulation converter is deployed. However, even with this feature, the other three common disadvantages of pre- and post-regulation converters exist. The first disadvantage is increased system cost and weight. This disadvantage becomes more prominent when the transferred power is increased. The second disadvantage is reduced PTE. The coupling coefficient and the input voltage of the post-regulation converter vary significantly in dynamic IPT applications. Therefore, the PTE of the converter is relatively low. The last disadvantage is decreased system reliability. An extra power stage needs to be inserted into the IPT system. This affects the reliability adversely, especially in the case of wide variation in input voltage. If a post-regulation converter is employed, energization of the control circuit is a significant challenge, especially at the startup stage. An extra dc–dc module, and a dedicated integrated chip (or a microprocessor) are required in this case.

Moreover, some investigations exploited variable inductor or capacitor for dynamic regulation of the output voltage or current. This, in essence, is a control strategy to achieve desirable performance [20], [21]. In addition to this particular control scheme, many other strategies are used in IPT systems. To the best of the authors' knowledge, control solutions are the final steps to obtain highly robust output voltage or current. The purpose of this paper is to derive the optimal values of the compensation parameters that would result in smallest voltage ripple without requiring any control circuit while the coupling and load are varied. Development of control scheme is not explored in this paper.

Theoretical analysis and experimental results in [8] indicate that the S/*CLC* compensation topology provides the characteristic of load-independent output voltage if the system is operated at the designed coupling coefficient. Even if the system is not operated at the designed coupling coefficient, the voltage deviation is quite small. This has been verified by Pspice simulation in the paper. The S/*CLC* topology also provides the advantages of loosely coupled transformer (LCT)-unconstrained output voltage, zero phase angle (ZPA), and zero voltage switching (ZVS) and requires relatively less compensation components. If the output voltage of an IPT system can be altered by only changing the compensation parameters, such as the S/*CLC*-compensated system in [8], the resulting IPT system is regarded as an LCT-unconstrained system, and it would provide the characteristic of LCT-unconstrained output voltage. In contrast, if the output voltage of an IPT system cannot be altered by only changing the compensation parameters, it can be altered by employing a new LCT with different parameters and by changing the compensation parameters, such as the S/SP-compensated system in [9]. This IPT system is regarded as an LCT-constrained system, which does not offer the characteristic of LCT-unconstrained output voltage. Considering the earlier discussion, S/*CLC* is chosen as the compensation topology in this paper.

Conventionally, the compensation parameters of the S/*CLC*-compensated IPT system are designed on the basis of *LC* (inductor-capacitor) resonance. However, the performance of the IPT system designed using conventional methods may not be optimal because the coupling and load change during operation. In order to obtain the optimal values of the compensation parameters, an exhaustive search algorithm can be adopted. Nevertheless, four parameters need to be determined, which means the number of the possible solutions is very large. In order to obtain a solution with sufficient accuracy, the count of the possible solutions for each parameter should be large enough. Assuming each parameter has 500 possible solutions, the number of the combination of the four parameters (each combination of the four parameters is a possible solution) is as large as 6.25×10^{10}. Therefore, it is impractical to derive the optimal solution with an exhaustive search algorithm. Compared to an exhaustive search algorithm, the particle swarm optimization (PSO) algorithm requires much smaller computation. In addition, it is relatively intuitive to understand and easy to implement. Therefore, this method is employed in this study to identify the optimal compensation parameters.

The remaining sections of this paper are organized as follows. Section II gives an overview of the S/*CLC* compensation topology. The circuit structures and the conventional parameter tuning methods are also introduced. The PSO algorithm is firstly explained in Section III. The details regarding the employment of PSO algorithm into the compensation parameter determination process are presented in this section as well. In order to illustrate the superiority of the PSO-based parameter design method, two systems, one designed with the PSO-based approach, and the other relying on conventional methods, are comprehensively compared in Section IV. The theoretical results are verified by a set of experiments. The prototype and the experiments are presented in Section V. In the final section, several conclusions are drawn.

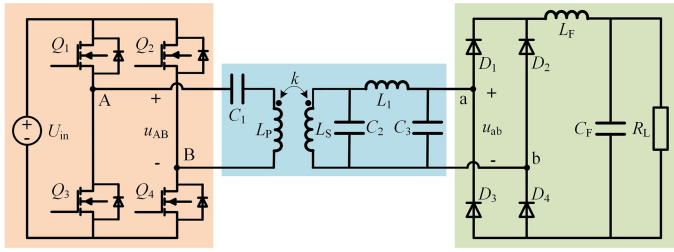

Fig. 2. Circuit diagram of an S/*CLC*-compensated IPT system.

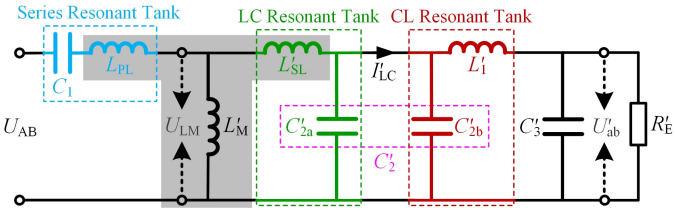

Fig. 3. Analytical circuit of the S/*CLC*-compensated IPT system.

II. Overview of the S/*CLC* Compensation Topology

Fig. 2 shows the circuit diagram of an S/*CLC*-compensated IPT system, which is mainly composed of three parts: 1) dc voltage source and full-bridge inverter; 2) compensation topology and LCT; and 3) rectifier, filter, and resistor (RFR). U_{in} is the dc input voltage. $Q_1 - Q_4$ are four switches, which form a full-bridge inverter. The instantaneous output voltage of the inverter is u_{AB}. C_1, C_2, L_1, and C_3 make up the S/*CLC* compensation topology. L_P, L_S, and k are the primary self-inductance, secondary self-inductance, and coupling coefficient of the LCT, respectively. $D_1 - D_4$ are four diodes, constituting a diode rectifier bridge. The instantaneous input voltage of the rectifier is u_{ab}. L_F and C_F are, respectively, filter inductor and capacitor. R_L is the resistive load.

Replacing the first part with an alternating current (ac) voltage source U_{AB} and substituting an ac equivalent resistance R_E for the third part, the analytical circuit of the S/*CLC*-compensated IPT system can be obtained, as shown in Fig. 3. The LCT in Fig. 2 is replaced by its T-type model, which is highlighted with gray shading. Here, L_{PL}, L'_{SL}, and L'_M are the primary leakage inductance, the secondary leakage inductance, and the mutual inductance, respectively. The parameters with the symbol "′" are referred to the primary side. U_{AB} and U'_{ab} are the root-mean-square (RMS) values of the fundamental harmonics of u_{AB} and u_{ab}, respectively. For simplicity, C'_2 is split into two parts as C'_{2a} and C'_{2b}. It is worth noting that the split is done mathematically, not physically. In practice, only one capacitor, C_2, is connected in parallel with L_S. The correlations between the parameters shown in Fig. 3 and those in Fig. 2 are given by (1), wherein α is the phase shift angle. It is set to zero in this paper. n denotes the equivalent turns ratio from the secondary to primary. Detailed

deduction of (1) is given in the Appendix

$$\begin{cases} U_{\mathrm{AB}} = \left[2\sqrt{2}\cdot\cos\left(0.5\alpha\right)\cdot U_{\mathrm{in}}\right]/\pi \\ n = \sqrt{L_S/L_P} \\ L_{PL} = L'_{SL} = \left(1-k\right)L_P \\ L'_M = kL_P \\ C'_2 = n^2 C_2 = C'_{2a} + C'_{2b} \\ L'_1 = L_1/n^2 \\ C'_3 = n^2 C_3 \\ U'_{ab} = \pi\cdot U_{RL}/\left(2\sqrt{2}\cdot n\right) \\ R'_E = \pi^2 R_L/\left(8n^2\right). \end{cases} \tag{1}$$

The equations for determining the compensation parameters are duplicated here for clarity

$$\begin{cases} L_1 = \left[\pi^2 U_{\mathrm{RL}}\left(1-k\right)\sqrt{L_P L_S}\right]/\left(8U_{\mathrm{in}}\right) \\ C_1 = 1/\left[{\omega_0}^2\left(1-k\right)L_P\right] \\ C_2 = 1/\left[{\omega_0}^2\left(1-k\right)L_S\right] + 1/\left({\omega_0}^2 L_1\right) \\ C_3 = \frac{kL_S C_2 + (1-k)L_S C_{2b}}{{\omega_0}^2 k L_1 L_P C_{2a}} - \frac{8L_S\tan(\theta)}{\pi^2\omega_0 L_P R_L}. \end{cases} \tag{2}$$

Here, U_{RL} is the desired dc voltage over the resistive load R_L. ω_0 is the system's operational angular frequency. θ is the designed input impedance angle. The expressions of C_{2a} and C_{2b} are given as follows:

$$\begin{cases} C_{2a} = 1/\left[{\omega_0}^2\left(1-k\right)L_S\right] \\ C_{2b} = 1/\left({\omega_0}^2 L_1\right) \end{cases}. \tag{3}$$

C_1 is tuned to resonate with L_{PL} at ω_0. C_1 and L_{PL} form the series resonant tank. C_{2a} is tuned to resonate with L_{SL} at ω_0. They make up the LC resonant tank, which converts the constant input voltage U_{LM} into constant output current I'_{LC}. C_{2b} is tuned to resonate with L_1 at ω_0. C_{2b} and L_1 constitute the CL resonant tank, which converts the constant input current I'_{LC} into constant output voltage U'_{ab}. C_3 is employed to adjust the input impedance. Detailed interpretation of the S/*CLC*-compensated IPT system can be found in [8].

III. Applying PSO into S/*CLC*-Compensated IPT Systems

It is impractical to derive the optimal solution of the four compensation parameters with an exhaustive search algorithm due to the requirement of extraordinarily large amount of computation. Hence, PSO algorithm is utilized in this paper. A brief introduction to the PSO algorithm and its application in this specific problem are given later.

A. Brief Introduction to PSO Algorithm

James Kennedy and Russell Eberhart first proposed the PSO method in 1995 [22], [23]. This approach was inspired by the Boids model presented in [24]. Later in 1998, Yuhui Shi and Russell Eberhart proposed a modified PSO by introducing inertia weight parameter in the original PSO to enhance its efficiency and effectiveness [25]. PSO algorithm is a stochastic evolution method that is based on swarm intelligence. It has been widely accepted as an efficient heuristic procedure for optimization problem in a continuous and multidimensional search space. It provides the advantages of fast convergence, lower computational cost, and insensitivity to the dimensions of the optimization problem [26]–[29]. A brief introduction to the fundamental operational principles of the PSO algorithm is given here.

The PSO algorithm is developed by simulating social behaviors. A population of individuals exists in the algorithm. In order to make the statement intuitive, these individuals are assumed to be a school of flying birds. These birds endeavor to find the global fittest position, which is the optimal solution of the problem, by cooperation and competition among the birds themselves through generations. Each bird adjusts its flying path in light of its own flying experience, and its companions' flying experience. Each bird is termed as a "particle," which is abstracted into a point in a *D*-dimensional space (solution space). The coordinates of the *i*th particle are represented by $X_I = (x_{i1}, x_{i2}, \ldots, x_{iD})$. They indicate the potential solution to the *D*-dimensional optimization problem. The best previous position (the position gives the best fitness value) of each particle is recorded and denoted as $p\mathrm{best}_I = (p_{i1}, p_{i2}, \ldots, p_{iD})$. The best previous position of all particles is recorded and represented as $g\mathrm{best} = (g_1, g_2, \ldots, g_D)$. Moreover, the rate of the position change, which is termed as velocity in PSO algorithm, for particle *i* is denoted as $V_I = (v_{i1}, v_{i2}, \ldots, v_{iD})$. The particles are manipulated using (4) and (5)

$$V_I(t+1) = \omega(t)V_I(t) + c_1 r_1\left[p\mathrm{best}_I(t) - X_I(t)\right] + c_2 r_2\left[g\mathrm{best}(t) - X_I(t)\right] \tag{4}$$

$$X_I(t+1) = X_I(t) + V_I(t+1) \tag{5}$$

where *t* is the current generation. ω is called the inertia weight parameter, which is varied with *t*. r_1 and r_2 are two random numbers uniformly distributed in the range of 0 and 1. c_1 and c_2 are two acceleration constants. The second part of (4) is the "cognition" part, which represents the private thinking of the particle itself. The third part of (4) is the "social" part, which represents the collaboration among the particles. Hence, c_1 is defined as the cognitive acceleration coefficient, while c_2 is defined as the social acceleration coefficient.

Equation (4) is used to calculate the particle's new velocity according to its previous velocity and the distances of its current position from its own best previous position and the group's best previous position. Then the particle flies toward a new position using (5). The velocity of each particle is constrained within the range $[V_{\min}\, V_{\max}]$, and the position is limited within the range $[X_{\min},\, X_{\max}]$. The performance of each particle is measured by a predefined fitness function, which is generally the optimization objective. The algorithm updates the equations iteratively until a predetermined maximum generation is met.

Fig. 4 gives a straightforward and intuitive description of the optimization process of PSO. The outermost circle (blue solid line) is the boundary of the *D*-dimensional solution space. $X_I(t)$ represents the position of particle *i*, while *t* stands for the current generation. T is the predetermined maximum generation. $g(t)$ denotes the global best position of all *t*th-generation particles. The global best positions are specially marked with small hollow

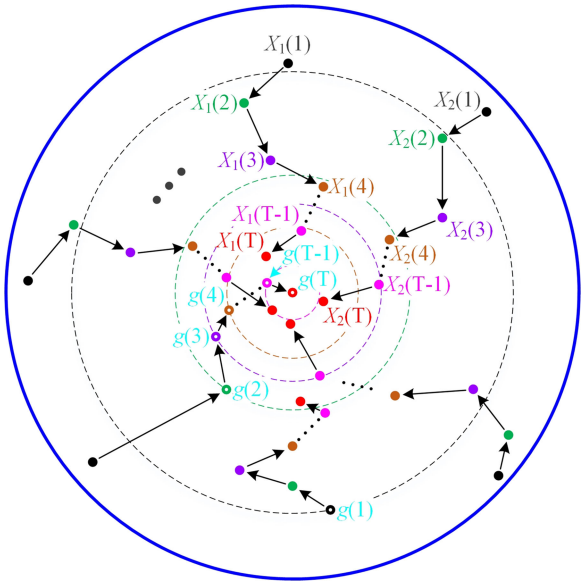

Fig. 4. Optimization process of PSO algorithm.

circles whereas the other positions are commonly marked with small solid circles. The color of the markers, both solid and hollow, indicates the generation of the particles. In particular, the black small circles denote the first-generation particles while the green small circles denote the second-generation particles, and so on. The evolution paths of six particles are given in Fig. 4. The evolution paths of other particles are not presented for the sake of brevity. The circle plotted with dashed line represents the boundary of the global best position of *t*th generation.

B. Applying PSO in Determining Compensation Parameters

1) Optimization Function: Four parameters (C_1, C_2, C_3, and L_1) need to be determined for an S/*CLC*-compensated IPT system. Therefore, determination of these parameters can be abstracted into a four-dimensional optimization problem. The optimization function is given as follows

$$F = \min\left[\sum_{i=1}^{N_k}\sum_{j=1}^{N_{\mathrm{RL}}}\left(f_U + f_{I1} + f_{I2} + f_{I3}\right)\right] + f_{\mathrm{ZVS}}(\theta) \quad (6)$$

where

$$f_U = \left\{U_{RL}\left[k(i), R_L(j)\right] - U_{RL-D}\right\}^2 \quad (7)$$

$$f_{I1} = \left\{I_{LP}\left[k(i), R_L(j)\right]/C_{\mathrm{adj-}LP}\right\}^2 \quad (8)$$

$$f_{I2} = \left\{I_{LS}\left[k(i), R_L(j)\right]/C_{\mathrm{adj-}LS}\right\}^2 \quad (9)$$

$$f_{I3} = \left\{I_{L1}\left[k(i), R_L(j)\right]/C_{\mathrm{adj-}L1}\right\}^2 \quad (10)$$

$$f_{\mathrm{ZVS}}(\theta) = \begin{cases} C_{\mathrm{pu}}, & \theta < 0^\circ \\ 0, & \theta \geq 0^\circ. \end{cases} \quad (11)$$

N_k and N_{RL} are the numbers of sampling points of the coupling coefficient k and resistive load R_L. The sampling intervals are set to be constant in this study. Therefore, the sampling intervals of k and R_L are $(k_{\max} - k_{\min})/(N_k - 1)$ and $(R_{L\max} - R_{L\min})/(N_{\mathrm{RL}} - 1)$, where $k_{\max}$, $k_{\min}$, $R_{L\max}$, and $R_{L\min}$ are the maximum and the minimum coupling coefficients and resistive loads, respectively. $k(i)$ and $R_L(j)$ stand for the ith k and the jth R_L, respectively. $U_{RL}[k(i), R_L(j)]$ represents the load voltage corresponding to a coupling coefficient of $k(i)$ and a resistive load of $R_L(j)$. U_{RL-D} is the designed load voltage, which is a predetermined constant. f_U is similar to the variance of the load voltage. However, f_U is not divided by the numbers of the sampling points. $I_{\mathrm{LP}}[k(i), R_L(j)]$, $I_{\mathrm{LS}}[k(i), R_L(j)]$, and $I_{L1}[k(i), R_L(j)]$ are the RMS currents flowing through L_P, L_S, and L_1, respectively. $C_{\mathrm{adj\text{-}LP}}$, $C_{\mathrm{adj\text{-}LS}}$, and $C_{\mathrm{adj\text{-}}L1}$ are the three adjustment constants. The bigger the adjustment constants, the lesser the importance of the corresponding current. θ is the input impedance angle. If θ is bigger than or equal to zero (which indicates an inductive load or a resistive load seen from the inverter), ZVS can be achieved. Otherwise, ZVS cannot be realized, and a punishment constant C_{pu} is added to the optimization function. In order to guarantee the achievement of ZVS operation, C_{pu} should be sufficiently large.

The optimization function contains three different objectives. The first objective is related to the load voltage ripple. The second objective is associated with the current stresses across the inductors. Finally, the third objective is to achieve ZVS operation. The current stresses across the inductors are involved in the optimization function because they greatly impact the PTE. The primary objective of this study is to develop an IPT system that ensures steady load voltage while the coupling and load change. However, the PTE should be kept at a relatively high level. Otherwise, the significance of this study will be compromised. The reason for including $f_{\mathrm{ZVS}}(\theta)$ in the optimization function is to attain higher PTE and to simplify the thermal design.

2) Determination of the Solution Space and Maximum and Minimum Velocities: The determination of the solution space is very important. If the space is too small, the optimal solution may not be included. If the space is too large, the search for the optimal solution will be difficult. According to the statement in [8], the performance of the S/*CLC*-compensated IPT system, which is tuned according to (2) and (3), is passable. Hence, the solution space of this study will be derived on the basis of the solution obtained with the conventional parameter tuning method. The solution space is determined as follows:

$$\begin{cases} C_{1-\min} = C_{1-\mathrm{con}}/C_{\mathrm{RA}-C1},\ C_{1-\max} = C_{\mathrm{RA}-C1}C_{1-\mathrm{con}} \\ C_{2-\min} = C_{2-\mathrm{con}}/C_{\mathrm{RA}-C2},\ C_{2-\max} = C_{\mathrm{RA}-C2}C_{2-\mathrm{con}} \\ C_{3-\min} = C_{3-\mathrm{con}}/C_{\mathrm{RA}-C3},\ C_{3-\max} = C_{\mathrm{RA}-C3}C_{3-\mathrm{con}} \\ L_{1-\min} = L_{1-\mathrm{con}}/C_{\mathrm{RA}-L1},\ L_{1-\max} = C_{\mathrm{RA}-L1}L_{1-\mathrm{con}} \end{cases} \quad (12)$$

where C_{1-con}, C_{2-con}, C_{3-con}, and L_{1-con} are the solutions obtained with the conventional parameter tuning method. $C_{\mathrm{RA\text{-}}C1}$, $C_{\mathrm{RA\text{-}}C2}$, $C_{\mathrm{RA\text{-}}C3}$, and $C_{\mathrm{RA\text{-}}L1}$ are the four constants determining the times that the corresponding parameters are reduced and amplified. They should be determined according to the practical constraints of the components of the compensation system. Take the compensation inductor for an example. Its inductance should be in a reasonable range. It cannot be extremely large because of constrains, such as cost, weight, and size. Meanwhile, it cannot

have a negative value, which disqualifies this as an inductor. The practical constraints of the compensation components are not very specific. Only general ranges of C_1, C_2, C_3, and L_1 can be determined. However, the proposed PSO-based method is insensitive to the solution space. The optimal solution can be acquired under a general solution space. C_{1-con}, C_{2-con}, C_{3-con}, and L_{1-con} can be calculated using (13). k_{ave} is the average coupling coefficient equaling $(k_{\text{min}} + k_{\text{max}})/2$. C_{3-con} is computed in the case of zero input impedance angle

$$\begin{cases} L_{1-\text{con}} = \left[\pi^2 U_{\text{RL}} \left(1-k_{\text{ave}}\right) \sqrt{L_P L_S}\right] / \left(8U_{\text{in}}\right) \\ C_{1-\text{con}} = 1/\left[{\omega_0}^2 \left(1-k_{\text{ave}}\right) L_P\right] \\ C_{2-\text{con}} = 1/\left[{\omega_0}^2 \left(1-k_{\text{ave}}\right) L_S\right] + 1/\left({\omega_0}^2 L_1\right) \\ C_{3-\text{con}} = \frac{{\omega_0}^2 k_{\text{ave}} (1-k_{\text{ave}}) L_1 {L_S}^2 C_2 + (1-k_{\text{ave}})^2 {L_S}^2}{{\omega_0}^2 k_{\text{ave}} {L_1}^2 L_P}. \end{cases} \tag{13}$$

The maximum and minimum velocities, V_{max} and V_{min}, are simply derived on the basis of the solution space. Without loss of generality, V_{min} is set to be the opposite of V_{max}. V_{max} is determined using (14). The velocities corresponding to the diverse compensation parameters are unequal because the ranges of these parameters are quite different. N_{C1}, N_{C2}, N_{C3}, and N_{C4} are the four positive integers. The greater N_{C1}, N_{C2}, N_{C3}, and N_{L1} are, the smaller the maximum velocities of the swarms, the poorer the capability of breadth search, and hence, the slower the convergence. However, greater N_{C1}, N_{C2}, N_{C3}, and N_{L1} indicate stronger capability of deep search as smaller maximum velocities are more beneficial to fine search in the vicinity of the current position. Therefore, moderate N_{C1}, N_{C2}, N_{C3}, and N_{L1}, neither very large nor very small, are more suitable for the proposed PSO-based method. The coefficient $\omega(t)$, which varies throughout the optimization, is employed to solve the contradiction between the capability of breadth and deep search. The expression of $\omega(t)$ will be given later

$$\begin{cases} V_{\text{max}-C1} = \left(C_{1-\text{max}} - C_{1-\text{min}}\right)/N_{C1} \\ V_{\text{max}-C2} = \left(C_{2-\text{max}} - C_{2-\text{min}}\right)/N_{C2} \\ V_{\text{max}-C3} = \left(C_{3-\text{max}} - C_{3-\text{min}}\right)/N_{C3} \\ V_{\text{max}-L1} = \left(L_{1-\text{max}} - L_{1-\text{min}}\right)/N_{L1}. \end{cases} \tag{14}$$

3) Variation of Inertia Weight Parameter Throughout the Optimization: As stated earlier, the inertia weight parameter, $\omega(t)$, is introduced into the PSO to enhance its efficiency and effectiveness. The time-variant inertia weight parameter is adopted in this study. The expression of $\omega(t)$ with respect to t is shown in (15). T is the predetermined maximum generation and t is the current generation. ω_{start} and ω_{end}, respectively, denote the start and the end inertia weight parameters

$$\omega\left(t\right) = \frac{T-t}{T} \cdot \left(\omega_{\text{start}} - \omega_{\text{end}}\right) + \omega_{\text{end}}. \tag{15}$$

4) Correction Law for Particle Velocity and Position: The velocity and position of the particle should be corrected if they are outside of their respective ranges. Diverse correction laws are employed in different studies. For the sake of clarity, the correction laws utilized in this paper are given as follows:

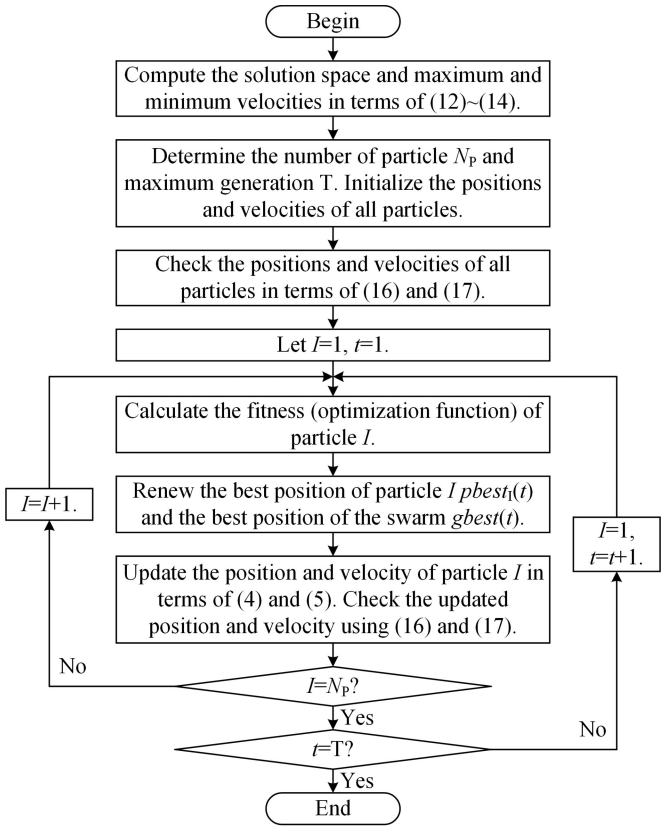

Fig. 5. Flowchart describing each step of the optimization.

$$V_{\text{corr}} = \begin{cases} V_{\text{max}}, V_{\text{orig}} > V_{\text{max}} \\ V_{\text{orig}}, V_{\text{min}} \le V_{\text{orig}} \le V_{\text{max}} \\ V_{\text{min}}, V_{\text{orig}} < V_{\text{min}} \end{cases} \tag{16}$$

$$X_{\text{corr}} = \begin{cases} X_{\text{max}}, X_{\text{orig}} > X_{\text{max}} \\ X_{\text{orig}}, X_{\text{min}} \le X_{\text{orig}} \le X_{\text{max}} \\ X_{\text{min}}, X_{\text{orig}} < X_{\text{min}}. \end{cases} \tag{17}$$

V_{corr} and X_{corr} represent corrected velocity and position, respectively, whereas V_{orig} and X_{orig} stand for original velocity and position. Every time the particle velocity and position are updated using (4) and (5), the resultant particle velocity and position should be checked instantly in terms of (16) and (17).

5) Complete Process of Applying PSO into Compensation Parameter Design: In order to make the optimization process clearer, a flowchart describing each step of the optimization is given in Fig. 5. Based on this flowchart, a MATLAB program is written and the optimal solution is subsequently derived. More details are presented in the next section.

Two aspects regarding the proposed PSO-based method need to be highlighted here. First, the results derived by the proposed method may be local optima because the IPT system is not proved to be a convex system. The optimization is highly complex, making the proof extremely difficult. The modified PSO algorithms and other intelligent algorithms with stronger

TABLE I
PARAMETERS RELATED TO SYSTEM DESIGN

Symbol	Value	Symbol	Value
U_{in}	50 V	k_{min}	0.2
f_0	85 kHz	k_{max}	0.4
$U_{RL\text{-}D}$	75 V	R_{Lmin}	50 Ω
L_P	103.79 μH	R_{Lmax}	100 Ω
L_S	104.12 μH	——	——

TABLE II
CONSTRAINTS RELATED TO THE PSO ALGORITHM

Symbol	Value	Symbol	Value	Symbol	Value
ω_{start}	0.9	$C_{adj\text{-}LS}$	10	$C_{RA\text{-}C3}$	6
ω_{end}	0.3	$C_{adj\text{-}L1}$	5	$C_{RA\text{-}L1}$	6
c_1	2	C_{pu}	5000	N_{C1}	200
c_2	2	N_P	60	N_{C2}	200
N_k	11	T	500	N_{C3}	200
N_{RL}	11	$C_{RA\text{-}C1}$	6	N_{L1}	200
$C_{adj\text{-}LP}$	10	$C_{RA\text{-}C2}$	6	——	——

capability of convergence to a global optimal position will be employed in the future. Second, the results derived by the proposed method are affected by initial condition and solver constraints. Therefore, the parameters utilized in the PSO algorithm should be adjusted to proper values. The optimization should be executed more than once, and the best solution among these optimized solutions should be ultimately selected. The influence of the initial condition can be significantly reduced by multiple optimizations.

IV. COMPARISON BETWEEN THE CONVENTIONAL AND PSO-BASED PARAMETER DESIGN METHODS

A. Practical Case

The parameters that are necessary for the system design are given in Table I. The range of the coupling coefficient varies in different applications. The maximum coupling coefficient in most IPT applications is no more than 0.5. The minimum coupling coefficient in medium- and high-power IPT applications is generally designed to be larger than 0.1 in order to obtain relatively high PTE. The range of coupling coefficient, from 0.2 to 0.4, is selected with various IPT systems incorporated. Substituting these parameters (as shown in Table I) into (13), L_{1-con}, C_{1-con}, C_{2-con}, and C_{3-con} can be calculated as 134.66 μH, 48.26 nF, 74.14 nF, and 73.24 nF, respectively.

The constants relating to the PSO algorithm utilized in this study are listed in Table II. In terms of (12), (14), and Table II, as well as previously obtained L_{1-con}, C_{1-con}, C_{2-con}, and C_{3-con}, the solution space and the maximum velocities are obtained. These are $C_1 \in [8.04, 289.56]$nF, $C_2 \in [12.36, 444.84]$nF, $C_3 \in [12.21, 439.44]$nF, $L_1 \in [22.44, 807.96]\mu H$, $V_{\text{max-}C1} = 1.41$ nF, $V_{\text{max-}C2} = 2.16$ nF, $V_{\text{max-}C3} = 2.14$ nF, and $V_{\text{max-}L1} = 3.93\,\mu$H.

For each set of system parameters, the input impedance angle, the load voltage, and the currents flowing through the three inductors can be readily calculated using fundamental circuit principles. The fitness (optimization function) can then be obtained. The profile of fitness with respect to particle generation is shown in Fig. 6. The original fitness is as large as 1.476×10^5, whereas the final fitness is only 701.7. It is evident that the compensation parameters have been remarkably optimized. The final compensation parameters are: $C_1 = 37.14$ nF, $C_2 = 107.35$ nF, $C_3 = 155.96$ nF, and $L_1 = 61.02\,\mu$H. It is very important to note the specific values of the fitness results presented in Fig. 6, including the original fitness of 1.476×10^5 and the optimized fitness of 701.7, are only applicable for the particular case. However, the downward trend of the fitness with respect to particle generation is applicable for all situations. Moreover, the optimized value of the fitness should be close to 707.1, at least at the same order of magnitude. It is highly possible that the original value of the fitness is quite different from 1.476×10^5. Nevertheless, it is very unlikely that the original value of the fitness is very small as the original positions of the swarms are randomly arranged.

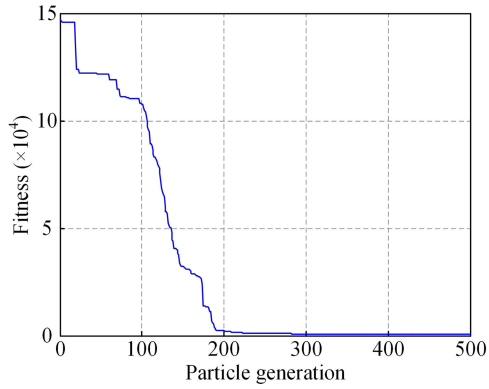

Fig. 6. Profile of fitness with respect to particle generation.

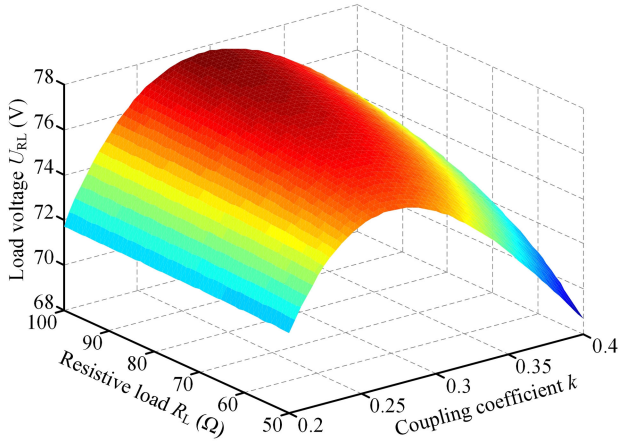

Fig. 7. Load voltage versus coupling coefficient and resistive load when the compensation parameters derived by the proposed PSO method are employed.

With the aforementioned four compensation parameters, as well as other necessary parameters listed in Table I, the load voltage versus coupling coefficient and resistive load can be acquired, as shown in Fig. 7. The minimum load voltage is 68.67 V when k and R_L are, respectively, 0.4 and 50 Ω. The maximum load voltage is 77.76 V when k and R_L are, respectively, 0.296 and 100 Ω. The voltage variation ripple (VVR) is only 6.21% when the coupling and load variation ratios are both

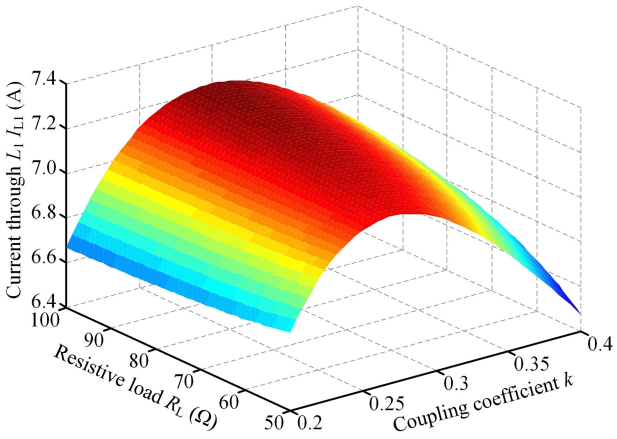

Fig. 8. Current flowing through L_1 versus coupling coefficient and resistive load when the compensation parameters derived by the proposed PSO method are employed.

200% (k increases from 0.2 to 0.4 while R_L increases from 50 to 100 Ω). The definition of VVR is given by (18), where $U_{\text{RL-max}}$ and $U_{\text{RL-min}}$ are the maximum and the minimum load voltages, respectively

$$\text{VVR} = \frac{U_{RL-\max} - U_{RL-\min}}{U_{RL-\max} + U_{RL-\min}} \times 100\%. \tag{18}$$

Fig. 8 exhibits the profile of I_{L1} versus k and R_L. The variation trends of I_{L1} with respect to R_L and k are highly similar to those of U_{RL}. I_{L1} reaches its maximum, 7.23 A, when R_L and k are 100 Ω and 0.296, respectively. This current is relatively large for a 110 W ($75^2/50 = 112.5$ W) IPT system. If the second part of the optimization function ($f_{I1} + f_{I2} + f_{I3}$) is not incorporated, the largest I_{L1} will be larger than 20 A. Hence, it can be concluded that the current flowing through L_1 is significantly reduced due to the inclusion of $f_{I1} + f_{I2} + f_{I3}$ in the optimization function. More importantly, I_{L1} can be further reduced using a smaller $C_{\text{adj-}L1}$. Nevertheless, it is achieved at the expense of bigger VVR. The main purpose of this study is to acquire an IPT system that exhibits high tolerance to misalignment and load variations. Therefore, $C_{\text{adj-}L1}$ is not set too small. Similar conclusions can be derived for I_{LP} and I_{LS}. However, due to space limitations, these are not discussed in detail.

B. Explanation for Low VVR

The VVR of the proposed IPT system versus the coupling coefficient and the load resistance is quite small, as shown in Fig. 7. A series of circuit diagrams are employed to explain the low VVR, as shown in Fig. 9. The dc voltage source and the full-bridge inverter in Fig. 2 are replaced by a sinusoidal voltage source U_{AB} in Fig. 9(a). Besides, the rectifier, the filter, and the resistor are substituted with an equivalent resistance R_E. Fig. 9(b) is the equivalent circuit of Fig. 9(a) where the LCT is substituted by its T-type model, and all the components in the secondary are referred to the primary. The Δ-shaped network in Fig. 9(b) (C'_2, L'_1, and C'_3) is transformed into the Y-shaped network in Fig. 9(c) (C'_{2-1}, L'_{1-1}, and C'_{3-1}). For the sake of clarity, both the Δ- and Y-shaped networks are circled

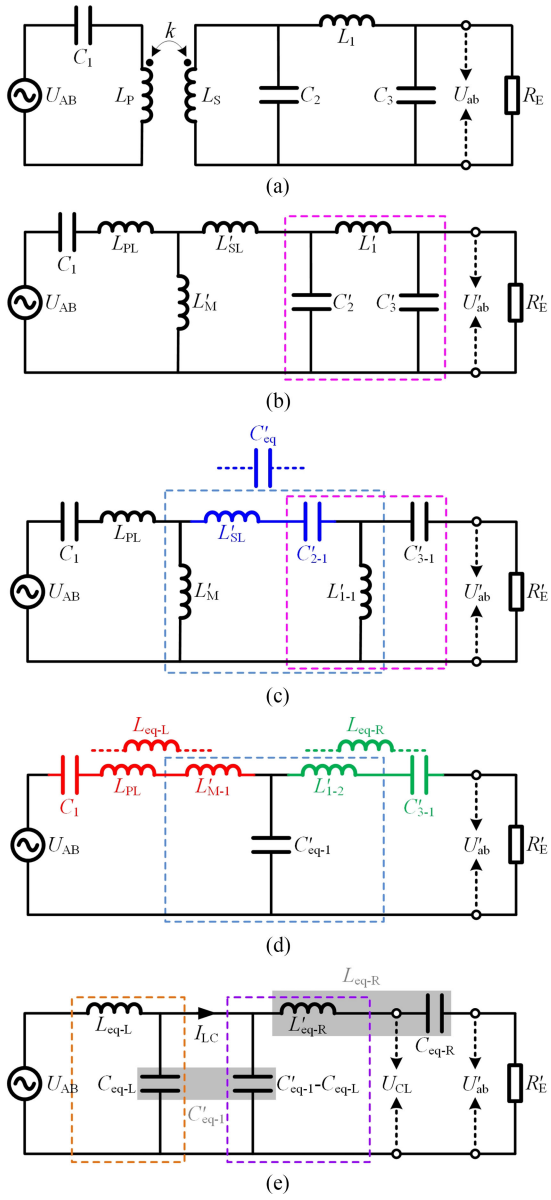

Fig. 9. Circuit diagrams to explain low VVR. (a) Simplified circuit of Fig. 2. (b) Equivalent circuit of (a) where all the components in the secondary are referred to the primary. (c) Equivalent circuit of (b) where the Δ-shaped network is substituted with a Y-shaped network. (d) Equivalent circuit of (c) where the Δ-shaped network is substituted with a Y-shaped network. (e) Equivalent circuit of (d) where the T-type network is replaced by LC and CL resonant networks.

by magenta dashed line. L'_{SL} and C'_{2-1} in Fig. 9(c) can be replaced by an equivalent capacitor C'_{eq}. The Δ connection of L'_M, C'_{eq}, and L'_{1-1} in Fig. 9(c) is further transformed into the Y connection of L'_{M-1}, C'_{eq-1}, and L'_{1-2} in Fig. 9(d). C_1, L_{PL}, and L'_{M-1} can be substituted by an equivalent inductor $L_{\text{eq-L}}$. L'_{1-2}, and C'_{3-1} can be substituted by an equivalent inductor $L_{\text{eq-R}}$. The T-type network in Fig. 9(d), which consists of $L_{\text{eq-L}}$, C'_{eq-1}, and $L_{\text{eq-R}}$, is then converted to LC ($L_{\text{eq-L}}$, $C_{\text{eq-L}}$) and CL ($C'_{eq-1} - C_{\text{eq-L}}$, $L'_{\text{eq-R}}$) resonant networks, as shown in Fig. 9(e). The total impedance of $L'_{\text{eq-R}}$ and $C_{\text{eq-R}}$ should equal the impedance of $L_{\text{eq-R}}$ in order to make the conversion valid.

The parameters of the LCT utilized in Fig. 9 are the same as those given in Table I, i.e., $L_P = 103.79\,\mu$H, $L_S = 104.12\,\mu$H, $k_{\min} = 0.2$, and $k_{\max} = 0.4$. The values of the four compensation parameters are identical to those derived with the proposed PSO method. C'_2, L'_1, C'_3, and C'_{2-1}, L'_{1-1}, C'_{3-1} are constant in the operation. Fig. 10(a) displays the impedance of $L_{\text{eq-L}}$, $L_{\text{eq-R}}$, and C'_{eq-1}, represented by $X_{\text{Leq-L}}$, $X_{\text{Leq-R}}$, and $X_{\text{C}}^{\prime eq-1}$, respectively, with respect to coupling coefficient. $X_{\text{Leq-L}}$, $X_{\text{Leq-R}}$, and $X_{\text{C}}^{\prime eq-1}$ all increase when the coupling coefficient is increased. The increase ratio of $X_{\text{C}}^{\prime eq-1}$ (25.19/12.59–1 = 100.08%) is very close to the increase ratio of $X_{\text{Leq-L}}$ (38.61/19.71–1 = 95.89%) when the coupling coefficient increases from 0.2 to 0.4. This is very important for the stability of U_{ab}.

The voltage gain of U_{CL} to U_{AB}, denoted as $G_{\text{CL/AB}}$, can be obtained as $C_{\text{eq-L}}/(C'_{eq-1} - C_{\text{eq-L}})$ in terms of the constant voltage to constant current (CV-CC) characteristic of the *LC* resonant network, and the constant current to constant voltage (CC-CV) characteristic of the *CL* resonant tank. The profile describing the variation of $G_{\text{CL/AB}}$ with respect to the coupling coefficient is shown in Fig. 10(b). $G_{\text{CL/AB}}$ almost does not vary when the coupling coefficient increases from 0.2 to 0.4. Therefore, U_{CL} keeps steady in the whole operating range of the coupling coefficient. The steady U_{CL} is resulted from close increase ratio of $X_{\text{C}}^{\prime eq-1}$ and $X_{\text{Leq-L}}$, in essence. It can be readily verified that U_{CL} will be constant regardless of the coupling coefficient if the increase ratio of $X_{\text{C}}^{\prime eq-1}$ is exactly equal to that of $X_{\text{Leq-L}}$.

U_{ab} can be yielded via dividing mod(- j$X_{\text{Ceq-R}} + R'_E$) by U_{CL} R'_{E}, where mod(·) represents the module of an impedance and $X_{\text{Ceq-R}}$ is the impedance of $C_{\text{eq-R}}$. The variation of the voltage division factor R_{VD}, defined as the ratio of R'_E to mod(- j$X_{\text{Ceq-R}} + R'_E$), versus coupling coefficient is also presented in Fig. 10(b). Owing to a relatively large value of R'_E, R_{VD} varies little when k increases from 0.2 to 0.4. The voltage gain of U_{ab} to U_{AB} ($G_{\text{ab/AB}}$) equals the product of $G_{\text{CL/AB}}$ and R_{VD}. It is also displayed in Fig. 10(b), and it hardly varies with the coupling coefficient. The three profiles in Fig. 10(b) are all acquired in the case of $R_L = 50\,\Omega$.

$G_{\text{CL/AB}}$ is irrelevant to the load resistance R_L, but R_{VD} and $G_{\text{ab/AB}}$ are associated with it. Fig. 10(c) and (d), respectively, present the variation of R_{VD} and $G_{\text{ab/AB}}$ versus coupling coefficient under different R_L. The variation of R_{VD} and $G_{\text{ab/AB}}$ becomes smaller when R_L is increased. In other words, the proposed IPT system provides better misalignment tolerance under the condition of greater load resistance. The VVR is quite small even though R_L lies in its minimum value (50 Ω). On the basis of the analysis presented earlier, it can be concluded that the low VVR is essentially resulted from close increase ratio of $X_{\text{C}}^{\prime eq-1}$ and $X_{\text{Leq-L}}$, as well as a relatively large value of R'_E in contrast to $X_{\text{Ceq-R}}$. It should be noted that the voltage gain $G_{\text{ab/AB}}$ does not equal the voltage gain $G_{\text{RL/in}}$, which is defined as the ratio of U_{RL} to U_{in}. Using (1), $G_{\text{RL/in}}$ equals the product of $G_{\text{ab/AB}}$ and $(8/\pi^2)$.

C. Comparison with the Conventional IPT System

The proposed IPT system is compared with the conventional system from three aspects: fitness, VVR, and PTE. The key

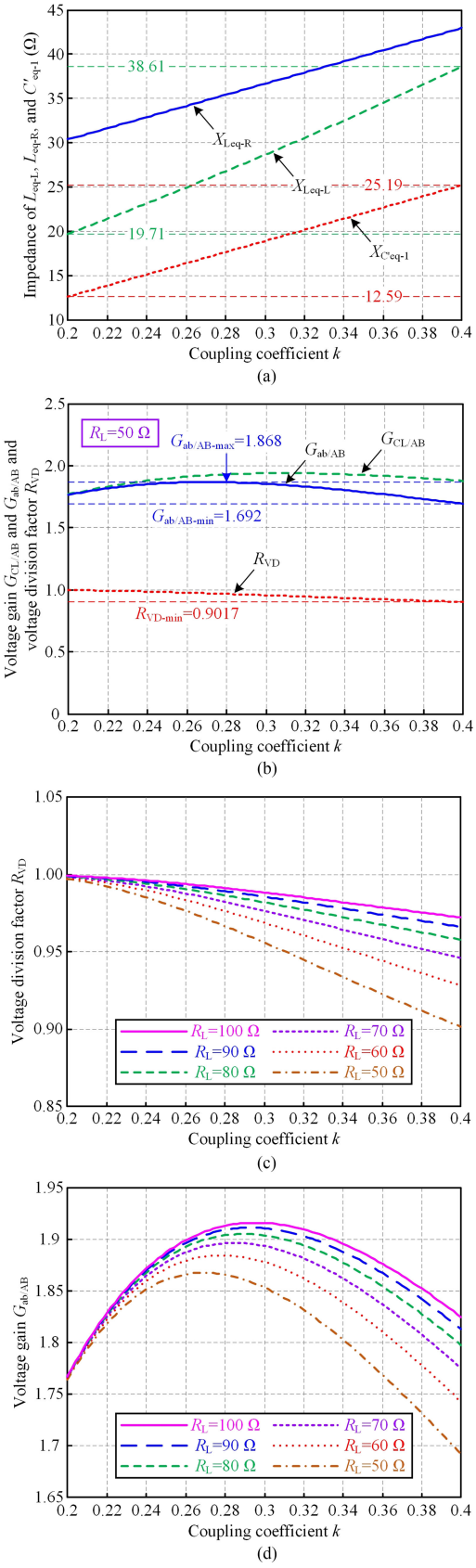

Fig. 10. Profiles associated with the VVR versus coupling coefficient. (a) Impedance of $L_{\text{eq-L}}$, $L_{\text{eq-R}}$, and C'_{eq-1}. (b) Voltage gains $G_{\text{CL/AB}}$ and $G_{\text{ab/AB}}$ and voltage division factor R_{VD}. (c) Voltage division factor R_{VD} under different R_L. (d) Voltage gain $G_{\text{ab/AB}}$ under different R_L.

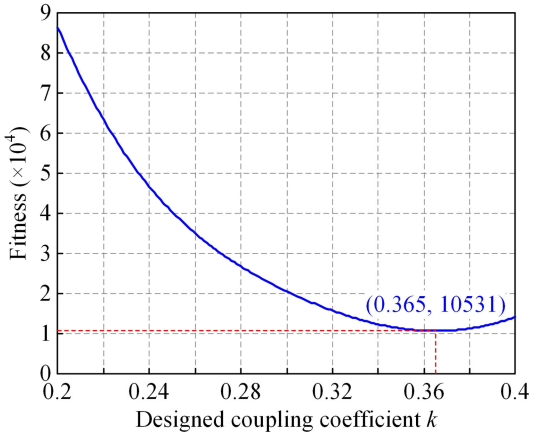

Fig. 11. Fitness of the conventional IPT system with respect to the designed coupling coefficient.

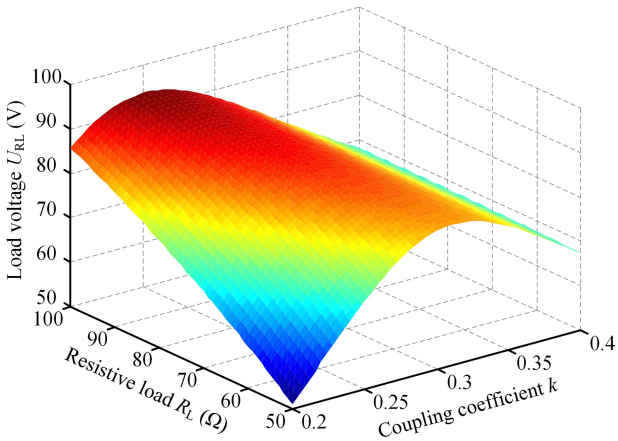

Fig. 12. Load voltage of the conventional IPT system with respect to coupling coefficient and resistive load.

parameters utilized in the conventional IPT system, including U_{in}, $U_{\text{RL-D}}$, f_0, L_P, L_S, k_{min}, k_{max}, $R_{L\text{min}}$, and $R_{L\text{max}}$, should be equal to those employed in the proposed IPT system. With regard to a particular designed coupling coefficient, the compensation parameters of the conventional IPT system can be computed using (2) and (3). The fitness can then be derived. Fig. 11 shows the fitness curves against the designed coupling coefficient. With the increase of the designed coupling coefficient, the fitness drops initially, and increases subsequently. The minimum fitness, 10 531, is obtained when the designed coupling coefficient is 0.365. Nevertheless, it is 15 times as large as the fitness of the proposed IPT system, implying significant performance improvements of the proposed system.

The load voltage of the conventional IPT system with respect to the coupling coefficient and resistive load is displayed in Fig. 12. The profile is obtained when the designed coupling coefficient equals 0.365. The highest load voltage, 93.69 V, is achieved when k and R_L are 0.256 and 100 Ω, respectively. The lowest load voltage, 50.99 V, is acquired when k and R_L are 0.2 and 50 Ω, respectively. In terms of (18), VVR is computed as 29.51%, which is 375.2% larger than its counterpart (6.21%).

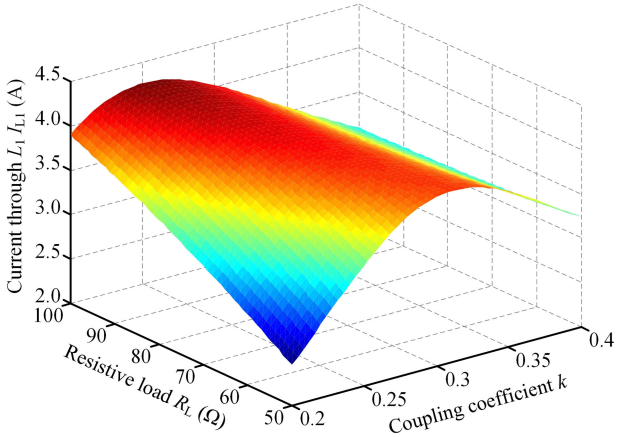

Fig. 13. Current flowing through L_1 of the conventional IPT system when the coupling coefficient and the resistive load are varied.

From this point of view, the proposed IPT system performs much better than the conventional IPT system.

Fig. 13 shows the current flowing through L_1 (I_{L1}) when the coupling coefficient and the resistive load are varied. The maximum and minimum values of I_{L1} are 4.26 and 2.45 A, respectively. On the one hand, the current stress across L_1 of the conventional system is smaller than that of the proposed system. On the other hand, the compensation inductance utilized in the conventional system (115.14 μH) is larger than that employed in the proposed system (61.02 μH). Consequently, the power loss of L_1 for these two systems are close. It is hard to obtain the accurate power loss of a ferrite-core inductor due to many complex factors, such as skin effect, proximity effect, and fringing effect. The efficiency comparison between these two systems is discussed in Section V.

V. Experimental Verification and Further Discussion

Two IPT prototypes are built to verify the correctness of the previously proposed theoretical analysis. One of them is designed with the conventional parameter design method, which is called the conventional prototype hereafter. The other is designed with the PSO-based method, and it is called the proposed prototype. Apart from the four compensation parameters, the remaining parameters of the conventional and the proposed prototypes are identical. Therefore, only the photo of the proposed prototype is given in Fig. 14. Two dc voltage sources are employed. One of them is used to power the drive circuit while the other is used to energize the main circuit. The primary drive printed circuit board (PCB) and the primary compensation PCB are separated in order to improve the flexibility of the prototype. A circular planar coil is utilized in this study as it is being employed in a wide range of applications globally.

The compensation parameters employed in the conventional and the proposed IPT systems are tabulated in Table III. In order to cancel out the voltage drop on various components, which are not incorporated in previous theoretical analysis, U_{in} is increased to 54 V in the verification experiments. The types of the inverter switch and the rectifier diode are SPW35N60CFD and MBR302000PT, respectively. The other key parameters,

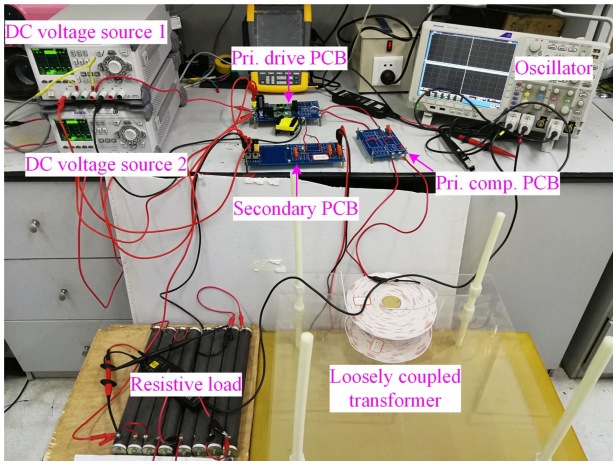

Fig. 14. Proposed prototype, where primary and compensation are abbreviated as pri. and comp., respectively.

TABLE III
KEY PARAMETERS EMPLOYED IN THE CONVENTIONAL AND PROPOSED IPT SYSTEMS

Symbol	Value in the conventional system	Value in the proposed system
C_1	53.3 nF	37.1 nF
C_2	81.8 nF	107.3 nF
C_3	71.2 nF	157.6 nF
L_1	122.4 μH	60.8 μH

including f_0, L_P, L_S, $k_{\min}$, $k_{\max}$, $R_{L\min}$, and $R_{L\max}$, are listed in Table I.

The voltage and current waveforms across each power stage of the proposed system are shown in Fig. 15. These waveforms are captured in the case that R_L and k equal 50 Ω and 0.2, respectively. The input and output voltage and current are shown in Fig. 15(a). The input and output power in this case is 126.4 and 97.3 W, respectively, indicating a PTE of 77%. Fig. 15(b) displays the gate-source and drain-source voltages of a MOSFET belonging to the lagging leg of the H-bridge inverter. $U_{\rm DS}$ decreases to zero before the increase of $U_{\rm GS}$. Therefore, ZVS operation is achieved. The output voltage of the inverter, as well as the voltage and current across L_P, is shown in Fig. 15(c). $I_{\rm LP}$ is relatively large for an IPT system whose input voltage and output power are 50 V and 110 W, respectively. This is attributed to a relatively large $C_{\text{adj-LP}}$. The most significant objective of this study is the lowest VVR against the variations in coupling coefficient and load resistance. Hence, $C_{\text{adj-LP}}$ is set to be relatively large. $I_{\rm LP}$ can be reduced by employing a smaller $C_{\text{adj-LP}}$. Fig. 15(d) displays the voltages and currents across L_S and L_1. $I_{\rm LS}$ is moderate, whereas I_{L1} is relatively large. The essential reason for large I_{L1} is relatively large $C_{\text{adj-}L1}$. $I_{\rm LS}$ can be reduced by utilizing a smaller $C_{\text{adj-}L1}$. However, the VVR versus coupling coefficient and load resistance will increase in this case.

The experimental results of the proposed system are shown in Figs. 16 and 17. With regard to a specific resistive load, the load voltage increases initially, and decreases later when the coupling coefficient is increased. The voltage variation

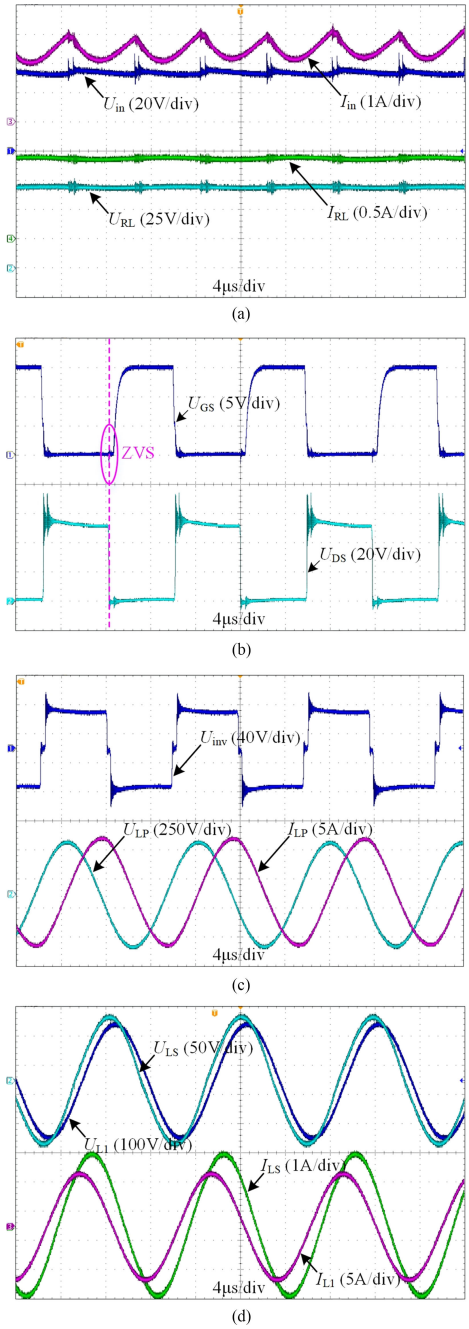

Fig. 15. Voltage and current waveforms across each power stage of the proposed system when R_L and k equal 50 Ω and 0.2, respectively. (a) Input and output voltage and current ($U_{\rm in}$, $I_{\rm in}$, U_{RL}, $I_{\rm RL}$). (b) Gate-source and drain-source voltages ($U_{\rm GS}$, $U_{\rm DS}$). (c) Output voltage of H-bridge inverter ($U_{\rm inv}$) and voltage and current across L_P ($U_{\rm LP}$, $I_{\rm LP}$). (d) Voltages and currents across L_S and L_1 ($U_{\rm LS}$, $I_{\rm LS}$, U_{L1}, I_{L1}).

($U_{RL\text{-max}} - U_{\text{RL-min}}$) is about 7 V when the coupling increases from 0.2 to 0.4. With regard to a specific coupling coefficient, the load voltage increases with the load. The voltage variation is around 4 V when the resistive load increases from 50 to 100 Ω. Using (18), the practical VVR can be computed as 6.61%, marginally larger than the theoretical value (6.21%). This mismatch is caused by measurement errors and parasitic parameters. The proposed prototype provides acceptable tolerance

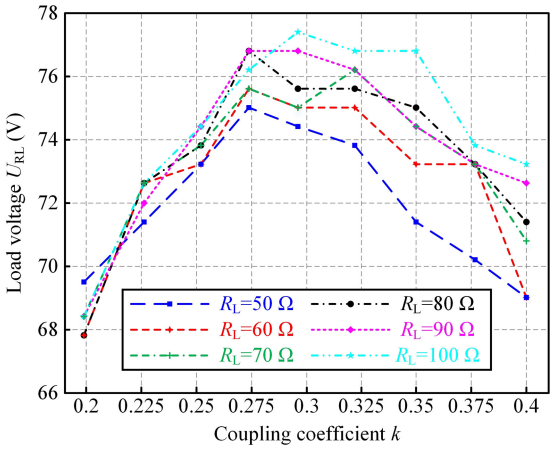

Fig. 16. Measured load voltage of the proposed IPT system against the coupling coefficient and resistive load.

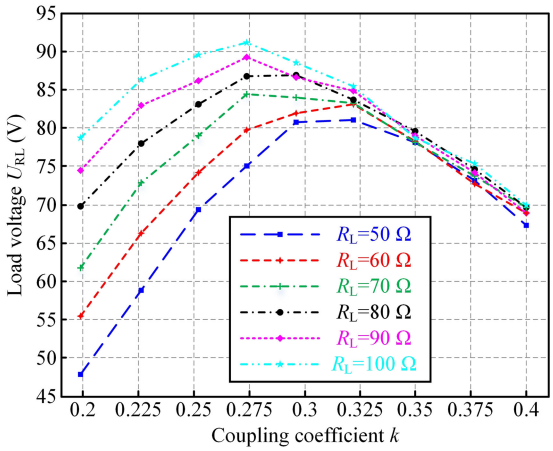

Fig. 18. Measured load voltage of the conventional IPT system with respect to coupling coefficient and resistive load.

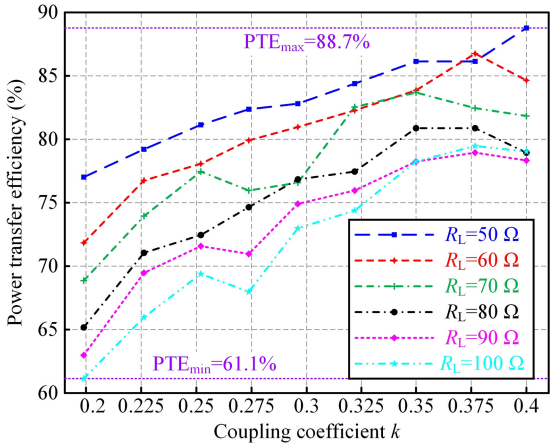

Fig. 17. Measured PTE of the proposed IPT system against coupling coefficient and resistive load.

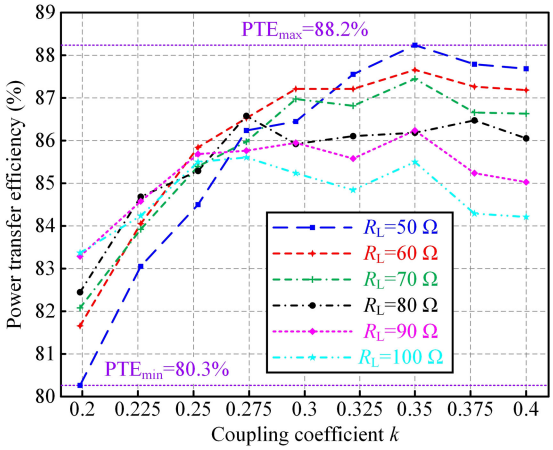

Fig. 19. Measured PTE of the conventional IPT system with respect to coupling coefficient and resistive load.

to coupling and load variations. The variation of load voltage is controlled within a small range even with 100% increase in both the coupling and the load. The experimental results agree well with the theoretical analysis. This demonstrates the effectiveness of the proposed PSO-based parameter design method.

Fig. 17 depicts the measured PTE of the proposed IPT system with respect to the coupling coefficient and resistive load. In general, the PTE increases with the coupling coefficient when the load is fixed, and it decreases with the load when the coupling coefficient is fixed. Hence, the maximum PTE (88.7%) is achieved when the load and the coupling coefficient are 50 Ω and 0.4, respectively. The minimum PTE (61.1%) is achieved when the load and the coupling coefficient are 100 Ω and 0.2, respectively. For a 110-W IPT system fed by a 50-V dc voltage source, the maximum PTE of 88.7% can be regarded as significantly high. The minimum PTE of 61.1% is also acceptable because the load power is only about 47 W (see Fig. 16). More importantly, the reduction of PTE is inevitable to keep the load voltage steady.

Similar experiments are also carried out on the conventional system. The results are shown in Figs. 18 and 19. The variation of the load voltage with respect to the coupling and the resistive load is similar to that of the proposed system. Two distinct differences can be observed by comparing Fig. 18 with Fig. 16. First, the voltage variation of the conventional system is much larger than that of the proposed system. The measured VVR of the conventional system is 31.22%, which is 372.3% larger than its counterpart in the proposed system. Second, for the conventional system, the load voltage rapidly increases with the load when the coupling coefficient is relatively small. On the contrary, for the proposed system, the load voltage rapidly increases with the load when the coupling coefficient is relatively large.

Fig. 19 displays the PTE of the conventional system against the coupling coefficient and the resistive load. In general, the PTE increases initially, and decreases later when the coupling coefficient is increased from 0.2 to 0.4. The highest PTE is achieved around the designed coupling coefficient (0.365). In the case of a relatively small coupling coefficient, PTE increases with R_L, but in the case of a relatively large coupling coefficient, PTE decreases with R_L. The biggest and smallest PTEs are 88.2% and 80.3%, respectively. PTE$_{max}$ of the conventional system is slightly lower than that of the proposed system.

However, PTE_{min} of the conventional system is much higher than that of the proposed system. Thus, the conventional system offers higher PTE than the proposed system. Despite this, the proposed system is regarded as a better choice because the large load voltage ripple of the conventional system can prohibit its employment in many fields. The most important performance index of this study is the load voltage ripple, rather than the PTE. Novel methods to increase the PTE of the proposed system will be exploited in near future.

The PSO-based parameter design method for an S/*CLC*-compensated IPT system can be employed in the applications where the coupling and the load change throughout the operation. The output voltage ripple can be significantly reduced using the proposed method. Therefore, in some applications where output voltage stability requirements are not strict, the post-regulation dc–dc converter can be removed. For instance, multifunctional cooktop, which can be used not only as a common induction cooker, but also as a wireless powered rice cooker. This is one typical example of such applications. The cost, weight, volume, and reliability of the proposed IPT system are superior to the conventional two-stage IPT systems. It is very important to note that the target application of the proposed method is not battery charging. The battery is generally charged in constant current mode first, and in constant voltage mode later. The IPT system designed with the proposed method does not have the characteristic of constant current output. Moreover, in order to extend the lifespan of a battery, the charging voltage should be very steady in constant voltage mode. The proposed IPT system cannot provide very steady output voltage in the case of large coupling variation.

The proposed method has two limitations. First, the output voltage ripple is not as small as desired when the coupling coefficient varies drastically. Second, the PTE is decreased when the proposed method is employed. These two limitations can be significantly improved by employing the proposed parameter design method in conjunction with magnetic coupling optimization. This is because smaller variation of coupling coefficient indicates lower output voltage ripple and higher PTE. The main reason for lower PTE of the proposed system is very high power loss on the compensation inductor. In order to improve the PTE, other compensation topologies without compensation inductor can be employed.

VI. Conclusion

In order to obtain an IPT system that provides high tolerance to both coupling and load variations, a novel PSO-based parameter design method is proposed in this article. It addresses the limitations of the conventional parameter design methods where the compensation capacitors/inductors are designed to resonate with certain other inductors/capacitors at the system's operational frequency. The S/*CLC* compensation topology is taken as an example in this study because it provides many desirable characteristics. However, it is very important to note that the proposed PSO-based method can be utilized in any compensation topology. Two comparative prototypes, one designed with the proposed method and the other with the conventional method, are built and tested. The measured VVR of the proposed system is only 6.61%, whereas the measured VVR of the conventional system is as high as 31.22%. In both cases, the coupling coefficient and the load resistance are doubled. The highest PTE of the proposed system is 88.7%. It is quite high for a 110-W IPT system as the input voltage is only 50 V. Experimental results show good agreement with the theoretical analysis, verifying the effectiveness of the proposed PSO-based method.

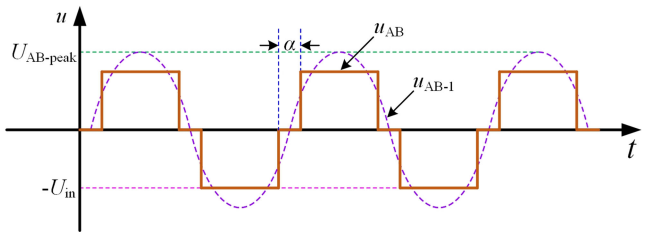

Fig. 20. Inverted input voltage u_{AB} and the fundamental harmonic of u_{AB} (u_{AB-1}).

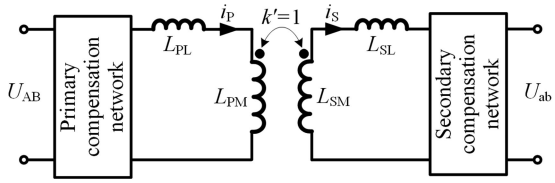

Fig. 21. Equivalent model of the LCT.

Appendix
Explanation and Derivation of (1)

U_{AB} is the RMS value of the fundamental harmonic of the inverted input voltage u_{AB}, as shown in Fig. 20. α represents the phase shift angle, which is also marked in Fig. 20. The expression of U_{AB} can be readily deduced via Fourier decomposition. More details regarding the derivation of U_{AB} can be found in [30].

Fig. 21 shows an equivalent model of the LCT. L_P is separated into two parts, L_{PL} and L_{PM}. They can be calculated using (19) and (20), respectively. L_{PL} represents the inductance generated by the leakage flux, while L_{PM} stands for the inductance resulted from the interlinkage flux. Similarly, L_S can also be split into two parts, L_{SL} and L_{SM}. They can be computed using (21) and (22), respectively. L_{SL} and L_{SM} are, respectively, the inductance attributed to the leakage and interlinkage flux. L_{PL} and L_{SL} are irrelevant to the coupling between the primary and secondary. They can be regarded as general inductance. L_{PM} and L_{SM} are fully coupled. A new parameter, k', is introduced to reflect the coupling between L_{PM} and L_{SM}. Apparently, it should equal one. L_{PM} and L_{SM} make up an ideal transformer. The turns ratio of the ideal transformer from the secondary to primary can then be obtained using (23). It is the same as the second expression of (1). L'_{SL}, L'_M, C'_2, L'_1, and C'_3 can be derived subsequently. The derivation of these five parameters is very straightforward.

Therefore, it is not presented in this paper

$$L_{\mathrm{PL}} = L_P\,(1-k) \tag{19}$$

$$L_{\mathrm{PM}} = L_P k \tag{20}$$

$$L_{\mathrm{SL}} = L_S\,(1-k) \tag{21}$$

$$L_{\mathrm{SM}} = L_S k \tag{22}$$

$$n = \sqrt{\frac{L_{\mathrm{SM}}}{L_{\mathrm{PM}}}} = \sqrt{\frac{L_S}{L_P}}. \tag{23}$$

The equivalent resistance of the RFR circuit, R_E, and the input voltage of the H-bridge diode rectifier U_{ab} are deduced in [31]. The expressions of R_E and U_{ab} are duplicated in (24) for convenient reading. R_E and U_{ab} are referred to the primary in this study. R_E should be divided by n^2 while U_{ab} should be divided by n. The last two expressions in (1) are verified as well

$$\begin{cases} R_E = \frac{\pi^2}{8} R_L \\ U_{\mathrm{ab}} = \frac{\pi}{2\sqrt{2}} U_{RL}. \end{cases} \tag{24}$$

REFERENCES

[1] Z. Li, C. Zhu, J. Jiang, K. Song, and G. Wei, "A 3-kW wireless power transfer system for sightseeing car supercapacitor charge," *IEEE Trans. Power Electron.*, vol. 32, no. 5, pp. 3301–3316, May 2017.

[2] W. X. Zhong and S. Y. R. Hui, "Maximum energy efficiency tracking for wireless power transfer systems," *IEEE Trans. Power Electron.*, vol. 30, no. 7, pp. 4025–4034, July 2015.

[3] S. R. Cove, M. Ordonez, N. Shafiei, and J. Zhu, "Improving wireless power transfer efficiency using hollow windings with track-width-ratio," *IEEE Trans. Power Electron.*, vol. 31, no. 9, pp. 6524–6533, Sept. 2016.

[4] S. Li, W. Li, J. Deng, T. D. Nguyen, and C. C. Mi, "A double-sided LCC compensation network and its tuning method for wireless power transfer," *IEEE Trans. Veh. Technol.*, vol. 64, no. 6, pp. 2261–2273, Jun. 2015.

[5] Y. Yao, Y. Wang, X. Liu, F. Lin, and D. G. Xu, "A novel parameter tuning method for double-sided LCL compensated WPT system with better comprehensive performance," *IEEE Trans. Power Electron.*, vol. 33, no. 10, pp. 8525–8536, Oct. 2018.

[6] Y. Wang, Y. Yao, X. Liu, D. Xu, and L. Cai, "An LC/S compensation topology and coil design technique for wireless power transfer," *IEEE Trans. Power Electron.*, vol. 33, no. 3, pp. 2007–2025, Mar. 2018.

[7] R. Mai, Y. Chen, Y. Zhang, N. Yang, G. Cao, and Z. He, "Optimization of the passive components for S-LCC topology based WPT system for charging massive electric bicycles," *IEEE Trans. Ind. Electron.*, vol. 65, no. 7, pp. 5497–5508, Jul. 2018.

[8] Y. Wang, Y. Yao, X. Liu, and D. Xu, "S/CLC compensation topology analysis and circular coil design for wireless power transfer," *IEEE Trans. Transp. Electrific.*, vol. 3, no. 2, pp. 496–507, Jun. 2017.

[9] J. Hou, Q. Chen, S. C. Wong, C. K. Tse, and X. Ruan, "Analysis and control of series/series-parallel compensated resonant converter for contactless power transfer," *IEEE J. Emerg. Sel. Topics Power Electron.*, vol. 3, no. 1, pp. 124–136, Mar. 2015.

[10] J. L. Villa, J. Sallan, J. F. Sanz Osorio, and A. Llombart, "High-misalignment tolerant compensation topology for ICPT systems," *IEEE Trans. Ind. Electron.*, vol. 59, no. 2, pp. 945–951, Feb. 2012.

[11] J. Zhao, T. Cai, S. Duan, H. Feng, C. Chen, and X. Zhang, "A general design method of primary compensation network for dynamic WPT system maintaining stable transmission power," *IEEE Trans. Power Electron.*, vol. 31, no. 12, pp. 8343–8358, Dec. 2016.

[12] S. Wang, J. Chen, Z. Hu, C. Rong, and M. Liu, "Optimisation design for series–series dynamic WPT system maintaining stable transfer power," *IET Power Electron.*, vol. 10, no. 9, pp. 987–995, 7 28 2017.

[13] M. Budhia, J. T. Boys, G. A. Covic, and C. Y. Huang, "Development of a single-sided flux magnetic coupler for electric vehicle IPT charging systems," *IEEE Trans. Ind. Electron.*, vol. 60, no. 1, pp. 318–328, Jan. 2013.

[14] A. Zaheer, D. Kacprzak, and G. A. Covic, "A bipolar receiver pad in a lumped IPT system for electric vehicle charging applications," in *Proc. IEEE Energy Convers. Congr. Expo.*, Raleigh, NC, USA, 2012, pp. 283–290.

[15] K. Aditya, V. K. Sood, and S. S. Williamson, "Magnetic characterization of unsymmetrical coil pairs using Archimedean spirals for wider misalignment tolerance in IPT systems," *IEEE Trans. Transp. Electrific.*, vol. 3, no. 2, pp. 454–463, Jun. 2017.

[16] Z. Zhang, H. Pang, C. H. T. Lee, X. Xu, X. Wei, and J. Wang, "Comparative analysis and optimization of dynamic charging coils for roadway-powered electric vehicles," *IEEE Trans. Magn.*, vol. 53, no. 11, pp. 1–6, Nov. 2017.

[17] X. Dai, L. Li, X. Yu, Y. Li, and Y. Sun, "A novel multi-degree freedom power pickup mechanism for inductively coupled power transfer system," *IEEE Trans. Magn.*, vol. 53, no. 5, pp. 1–7, May 2017.

[18] R. Carta and R. Puers, "Wireless power and data transmission for robotic capsule endoscopes," in *Proc. 18th IEEE Symp. Commun. Veh. Technol. Benelux*, Ghent, 2011, pp. 1–6.

[19] S. Y. Choi, J. Huh, W. Y. Lee, and C. T. Rim, "Asymmetric coil sets for wireless stationary EV chargers with large lateral tolerance by dominant field analysis," *IEEE Trans. Power Electron.*, vol. 29, no. 12, pp. 6406–6420, Dec. 2014.

[20] N. Keeling, G. A. Covic, F. Hao, L. George, and J. T. Boys, "Variable tuning in LCL compensated contactless power transfer pickups," in *Proc. IEEE Energy Convers. Congr. Expo.*, San Jose, CA, USA, 2009, pp. 1826–1832.

[21] E. S. Lee, B. G. Choi, J. S. Choi, D. T. Nguyen, and C. T. Rim, "Wide-range adaptive IPT using dipole-coils with a reflector by variable switched capacitance," *IEEE Trans. Power Electron.*, vol. 32, no. 10, pp. 8054–8070, Oct. 2017.

[22] J. Kennedy and R. Eberhart, "Particle swarm optimization," in *Proc. IEEE Int. Conf. Neural Netw.*, Perth, WA, USA, 1995, vol. 4, pp. 1942–1948.

[23] R. Eberhart and J. Kennedy, "A new optimizer using particle swarm theory," in *Proc. Proc. 6th Int. Symp. Micro Machine Human Sci.*, Nagoya, 1995, pp. 39–43.

[24] C. W. Reynolds, "Flocks, herds and schools: A distributed behavioral model," *Comput. Graph.*, vol. 21, no. 4, pp. 25–34, Aug. 1987.

[25] Y. Shi and R. Eberhart, "A modified particle swarm optimizer," in *Proc. IEEE Int. Conf. Evol. Comput. IEEE World Congr. Comput. Intell. (Cat. No. 98TH8360)*, Anchorage, AK, USA, 1998, pp. 69–73.

[26] J. H. Lee, J. Y. Song, D. W. Kim, J. W. Kim, Y. J. Kim, and S. Y. Jung, "Particle swarm optimization algorithm with intelligent particle number control for optimal design of electric machines," *IEEE Trans. Ind. Electron.*, vol. 65, no. 2, pp. 1791–1798, Feb. 2018.

[27] M. Collotta, G. Pau, and V. Maniscalco, "A fuzzy logic approach by using particle swarm optimization for effective energy management in IWSNs," *IEEE Trans. Ind. Electron.*, vol. 64, no. 12, pp. 9496–9506, Dec. 2017.

[28] T. S. Babu, J. P. Ram, T. Dragičević, M. Miyatake, F. Blaabjerg, and N. Rajasekar, "Particle swarm optimization based solar PV array reconfiguration of the maximum power extraction under partial shading conditions," *IEEE Trans. Sustain. Energy*, vol. 9, no. 1, pp. 74–85, Jan. 2018.

[29] Q. Zhang, W. Liu, X. Meng, B. Yang, A. V. Vasilakos, "Vector coevolving particle swarm optimization algorithm," *Inf. Sci.*, vol. 394–395, pp. 273–298, 2017.

[30] A. V. Oppenheim, A. S. Willsky, and S. Hamid Nawab, "Fourier series representation of periodic signals," in *Signals and Systems*, 2nd ed. Upper Saddle River, NJ, USA: Prentice-Hall, 1996, pp. 177–284.

[31] R. L. Steigerwald, "A comparison of half-bridge resonant converter topologies," *IEEE Trans. Power Electron.*, vol. 3, no. 2, pp. 174–182, Apr. 1988.

Yousu Yao (S'18) was born in Huai'an, Jiangsu, China, in 1991. He received the B.S. degree in electrical engineering in 2014 from the Harbin Institute of Technology, Harbin, China, where he is currently working toward Ph.D. degree.

His current research interests include inductive power transfer, magnetic coupling structure design, and wireless power and data transmission.

Dr. Yao the recipient of the Best Paper Award from the 2017 IEEE Transportation Electrification Conference and Expo, Asia-Pacific (ITEC-AP 2017).

Yijie Wang (S'09–M'15–SM'15) was born in Heilongjiang Province, China, in 1982. He received the B.S., M.S., and Ph.D. degrees in electrical engineering from the Harbin Institute of Technology, Harbin, China, in 2005, 2007, and 2012, respectively.

From 2012 to 2014, he was a Lecturer, and from 2014 to 2017, he was an Associate Professor with the Department of Electrical and Electronics Engineering, Harbin Institute of Technology, where since 2017, he has been a Professor. His current interests include dc–dc converters, soft-switching power converters, power factor correction circuits, digital control electronic ballasts, and LED lighting systems. He is an Associate Editor of the *IET Power Electronics* and the *Journal of Power Electronics*.

Dr. Wang is an Associate Editor of the IEEE TRANSACTIONS ON INDUSTRIAL ELECTRONICS, the IEEE JOURNAL OF EMERGING AND SELECTED TOPICS IN POWER ELECTRONICS, and the IEEE ACCESS.

Xiaosheng Liu (M'14) was born in Qiqihar, Heilongjiang, China, in 1966. He received the B.S. and M.S. degrees in electrical engineering and the Ph.D. degree in mechatronics engineering, all from the Harbin Institute of Technology, Harbin, China, in 1988, 1993, and 1999, respectively.

Since 2006, he has been a Professor with the Department of Electrical Engineering, Harbin Institute of Technology. His current research interests include power line communication and its routing methods, communication networks and control technology, and information and communication of smart grids.

Yu Pei was born in Kangping, Liaoning, China, in 1995. He received the B.S. degree in electrical engineering in 2017 from the Harbin Institute of Technology, Harbin, China, where he is currently working toward the M.S. degree in electrical engineering.

His current research interests include wireless power transfer, magnetic coupling structure design, and closed-loop control.

Dianguo Xu (M'97–SM'12–F'17) received the B.S. degree in control engineering from the Harbin Engineering University, Harbin, China, in 1982, and the M.S. and Ph.D. degrees in electrical engineering from the Harbin Institute of Technology (HIT), Harbin, in 1984 and 1989, respectively.

In 1984, he joined the Department of Electrical Engineering, HIT, as an Assistant Professor. Since 1994, he has been a Professor in the Department of Electrical Engineering, HIT. He was the Dean of School of Electrical Engineering and Automation, HIT, from 2000 to 2010. He is now the Vice President of HIT. His current research interests include renewable energy generation technology, power quality mitigation, sensorless vector-controlled motor drives, and high-performance PMSM servo system. He has authored or coauthored over 600 technical papers.

Dr. Xu is an Associate Editor of the IEEE TRANSACTIONS ON INDUSTRIAL ELECTRONICS, the IEEE TRANSACTIONS ON POWER ELECTRONICS, and the IEEE JOURNAL OF EMERGING AND SELECTED TOPICS IN POWER ELECTRONICS. He is the Chairman of the IEEE Harbin Section. He is the recipient of the 2018 IEEE Industry Applications Society Outstanding Achievement Award.

Xiufang Liu was born in Shenyang, Liaoning, China, in 1982. She received the B.S. and M.S. degrees in mechanical design and theory from the Northeastern University, Shenyang, China, in 2003 and 2006, respectively.

She is currently an Engineer in Shanghai Aerospace Equipment Manufacturer Co., Ltd, Shanghai, China. Her current research interests include ground test equipment (GTE) and novel sensors.